Seasonal Water Transport in the Atmosphere of Mars: Applications of a Mars General Circulation Model using Mars Global Surveyor Data

Jeffery L. Hollingsworth[*][†], Alison F. C. Bridger[b] & Robert M. Haberle[†]

University Consortium Agreement: NCC2-5230
Project Duration: 1 July 1997–30 June 1999 (30 November 1999 with 5 month no-cost extension)

[*]San Jose State University Foundation, P.O. Box 720130, San Jose, California 95172, USA
[†]NASA Ames Research Center, MS: 245-3, Moffett Field, California 94035, USA
[b]Department of Meteorology, San Jose State University, San Jose, California 95192, USA

ABSTRACT

This is a Final Report for a Joint Research Interchange (JRI) between NASA Ames Research Center and San Jose State University, Department of Meteorology. We present below a summary of progress made during the duration of this JRI. The focus of this JRI has been to investigate seasonal water vapor transport in the atmosphere of Mars and its effects on the planet's present climate. To this end, the primary task has been to adapt a new dynamical processor for the adiabatic tendencies of the atmospheric circulation into the NASA Ames Mars general circulation model (MGCM). Using identical boundary and initial conditions, several comparative tests between the new and old MGCMs have been performed and the nature of the simulated circulations have been diagnosed. With confidence that the updated version of the Ames MGCM produces quite similar mean and eddy circulation statistics, the new climate model is well poised as a tool to pursue fundamental questions related to the spatial and seasonal variations of atmospheric water vapor on Mars, and to explore exchanges of water with non-atmospheric reservoirs and transport within its atmosphere. In particular, the role of surface sources and sinks can be explored, the range of water-vapor saturation altitudes can be investigated, and plausible precipitation mechanisms can be studied, for a range of atmospheric dust loadings. Such future investigations can contribute to a comprehensive study of surface inventories, exchange mechanisms, and the relative importance of atmospheric transport Mars' water cycle. A listing of presentations made and manuscripts submitted during the course of this project is provided.

1. INTRODUCTION

Of the three climate cycles, carbon dioxide, dust and water, the water cycle on Mars is undoubtedly the least well understood. Observations gathered during the Viking spacecraft missions have provided clear evidence that Mars exhibits an active hydrological cycle. The best description of this cycle is given by data collected during the Viking spacecraft era from the Mars Atmospheric Water Detector

(MAWD) experiment [*Farmer et al.*, 1977; *Jakosky and Farmer*, 1982] which offer a global view of spatial and seasonal variations in the column abundance of water vapor for just over one Mars year [*Jakosky*, 1985]. The MAWD experiments consisted of near-infrared reflectance spectrometers at a wavelength near 1.4 μm (7230 cm^{-1}). Along the observational path, the relative absorption in three separate, closely adjacent water bands and two continuum bands were measured, which were then translated into column abundances using the viewing geometry of the spacecraft [cf. *Farmer et al.*, 1977].

The globally and annually averaged column abundance of water vapor on Mars has been determined to be about 10–15 precipitable microns (pr μm), where 100 pr μm corresponds to 10^{-2} g cm^{-2} [*Jakosky*, 1985]. Furthermore, a pronounced seasonal cycle and hemispheric asymmetry in the atmospheric water vapor content have been detected. In longitudinally averaged data, the largest values, $O(100$ pr μm$)$, occur over the north polar region near $L_s = 120°$, or just following northern summer solstice. (Here, L_s denotes the solar aerocentric longitude, with $0°$ corresponding to northern spring equinox; $90°$ northern summer solstice; and so forth.) During southern summer, the largest water abundance occur at 60°S latitude nearly exactly at solstice, although a factor of six less than those seen during northern summer. That the southern hemisphere peak values are weaker may be, in part, due to the effects of atmospheric dust (very enhanced dust loading occurred over the entire globe at this season) which can reduce the apparent abundance by scattering of light [*Farmer et al.*, 1977].

In addition to MAWD observations, separate thermal infrared observations made from Viking have been used to deduce that the north polar region contains a water-ice (residual) polar cap. With surface temperatures near 200 K, this water-ice cap is exposed following the sublimation and retreat of the seasonal CO_2 cap during northern summer. Conversely, the weak abundance values in high southern latitudes together with thermal measurements [*Kieffer*, 1979], suggest (at least during the Viking years) that the southern polar region stays near the CO_2 condensation temperature, never exposing a water-ice reservoir during southern summer. Despite a seasonal retreat of the CO_2 cap boundary, the southern residual polar cap, can thus act as an efficient cold trap for water vapor in the atmosphere.

More recently, Hubble Space Telescope (HST) observations of Mars during late spring ($L_s = 63.5°$) made in the violet and ultraviolet [*James et al.*, 1996] have shown considerable cloudiness in the sub- and extra-tropics over the entire globe. Visible opacities range between 0.2–0.5, and with assumed mean particle sizes of 1–2 μm, the water reservoir associated with this encircling belt of clouds has been estimated to be $O(1$ pr μm$)$. This is to be compared with a $O(10$ pr μm$)$ column abundance at this season from the MAWD data [*Jakosky*, 1985].

It is most certain that both polar caps, with temperatures near the CO_2 sublimation temperature (150 K) during winters, act as a sink for water vapor. Yet during the summer, the north cap can act as source and the south cap can act as a sink, resulting in, over a year, a net loss of water from the north cap and a net gain onto the south cap. This hemispheric asymmetry suggests a net transfer of water from the north to the south during the current epoch [*Jakosky*, 1985]. Because of the potential for large interannual variations and the rather uncertain role of atmospheric transport, the nature of this transfer remains far from well understood [*Jakosky and Haberle*, 1992].

Applying a simplified Mars global circulation model, *Houben et al.* [1997] investigated atmospheric water vapor transport, and the relative importance of surface sources and sinks in the observed water cycle. The model used, however, neglected the diurnal cycle (i.e., the atmospheric response to daily radiative forcing) and the effects of large-scale topography. To force the atmospheric circulation, simple representations of the thermal and mechanical driving were invoked. Coupled to the circulation model was an aerosol model which carried out transport calculations "off line" from winds and temperatures provided by the circulation model. Also included was a parameterization of subsurface regolith adsorption. Results of this study have suggested the importance on the water cycle of a thin

adsorbing layer within the regolith which can effectively limit low-level atmospheric relative humidity and prevent the growth of widespread ice deposits in low latitudes. Because of its full global geometry, the allowance for longitudinally varying, and developing and decaying wave motions (i.e., midlatitude transient eddies or "weather systems"), and the inclusion of near-surface exchange processes, the investigation of *Houben et al.* [1997] has offered vast improvements over most models used to date in Mars water vapor transport studies [*Jakosky and Haberle,* 1992].

However, as the coupled transport-circulation model conducted by *Houben et al.* [1997] lacked the effects of surface topography and a realistic diurnal cycle, some circulation components were necessarily absent in the simulations. For example, subtropical low-level jets (i.e., the near-surface return branch of the Hadley circulation [*Joshi et al.,* 1995; *Joshi et al.,* 1997]) and their longitudinal confinement on the eastern slopes of Tharsis and Arabia Terra could not simulated. In middle latitudes, large-scale, vertically deep, quasi-stationary planetary waves [*Hollingsworth and Barnes,* 1996]—waves that can profoundly influence the development, decay and geographic "localization" of Mars' midlatitude weather systems [*Hollingsworth et al.,* 1996; 1997a; 1997b]—were also missing in the *Houben et al.* [1997] study. Such circulation components will undoubtedly have a significant effect on the net transport circulation in both the sub- and extra-tropics. Furthermore, the subsurface regolith model assumed globally uniform soil adsorption and thermal properties (e.g., soil density, porosity, thermal conductivity, etc.).

To improve on the modeling efforts performed to date, we originally proposed to apply the most recent version of the NASA Ames Mars general circulation model (MGCM) to investigate Mars' water cycle. Atmospheric general circulation models are based on the equations of motion for the time evolution of the full 3D flow field and of the thermodynamic state of the atmosphere. In these most sophisticated climate models, the set of equations, referred to as the meteorological primitive equations (PE) [*Holton,* 1992], includes detailed complex physics for "right hand side" terms in the system (e.g., radiative-transfer physics yielding explicit diabatic heating rates). As such, these global climate models can be computationally very intensive.

Before investigations of Mars' water cycle can be accomplished using the Ames MGCM, an assessment of fundamental changes and various improvements to the model [*Haberle et al.,* 1997b; *Haberle et al.,* 1999] needs to be performed. This has been the primary goal of the research conducted under this JRI. Most recently is the adaptation of a new "dynamical core" which computes the adiabatic tendencies of atmospheric mass, momentum and temperature. Several simulations have been conducted to assess how the new dynamical processor based on the Arakawa "C"-grid (i.e., the explicit staggering of momentum, temperature, pressure, and vorticity on a discrete grid in the horizontal direction for each atmospheric layer), performs compared to the old version of the Ames MGCM dynamical core based on the Arakawa "B-"grid [*Arakawa and Lamb,* 1977]. Simulations using identical "simple physics" parameterizations, as well as the full-physics package of the MGCM have been performed. A variety of climate statistics (e.g., time-mean flows and eddy fields) have been compared for realistic solstitial mean basic states. Results of this research have demonstrated that the new Ames MGCM produces rather similar circulation statistics for first-, second- and higher-order order meteorological fields, and that, a tendency for convergence of numerical solutions is apparent. Future research will then apply the new model in studies of Mars' water cycle and the mechanisms of atmospheric transport associated with various circulation components.

Prior to presenting key results of this investigation, a brief summary of the current Ames MGCM is outlined below.

The NASA Ames Mars General Circulation Model (MGCM)

The MGCM is a 3D global atmospheric model based on the meteorological primitive equations in spherical coordinates. These equations account for momentum, mass and thermodynamic energy balances, plus a gas equation of state. Dependent variables are staggered in the horizontal and vertical directions, and the spatial and temporal finite differencing scheme conserves energy and mean square enstrophy. The model uses a terrain-hugging vertical coordinate ($\sigma = (p - p_T)\Pi^{-1}$ where $\Pi = p_s - p_T$, p_T = the "tropopause" (model top) pressure, and p_s = the surface pressure), whereby spatially varying topography at the model's surface can be handled correctly. Nominal resolution of the MGCM is $9 \times 7.5°$ longitude and latitude, respectively, with 16–30 vertical levels (denoted an L16 or L30 configuration) extending up to approximately 60–110 km. The MGCM's heating routines allow for a diurnal cycle, a surface heat budget, radiative effects of CO_2 gas and suspended aerosols (e.g., dust and/or water condensate), latent heat release associated with CO_2 condensation, and heat exchange between the atmosphere and surface. The boundary layer parameterization of the MGCM has been improved recently in that frictional forces and turbulent heating are treated as diffusion processes. The local (i.e., Richardson number and mixing length) dependent eddy coefficients are taken from the level-2 formalism of *Mellor and Yamada* [1982]. Near the model top, a Rayleigh friction "sponge layer" is applied to help dissipate upward propagating waves and spurious downward reflection of wave energy. Optionally, a gravity-wave scheme essentially similar to one used in terrestrial global models [*Rind et al.*, 1988a; 1988b] has been incorporated. To save computational time, radiative fluxes are computed using look-up tables created off line using a CO_2 line-by-line code and a multi-spectral doubling code for dust. Further documentation on the nature of Mars' climate as simulated by the MGCM and details of the MGCM's physical processes are provided in *Pollack et al.* [1990]; *Haberle et al.* [1993]; *Haberle et al.* [1997b]; and *Haberle et al.* [1999]. Details of the new dynamical core based on the Arakawa "C"-grid is provided in *Suarez and Takacs* [1995].

2. KEY RESULTS OF INVESTIGATION

By performing a series of carefully designed fixed-season simulations, as well as annual simulations, the primary objective of this research proposal has been to systematically evaluate the atmospheric circulation and climate of Mars as simulated by the new and old versions of the Ames MGCM. A secondary objective of this proposal has been to initiate the movement toward "validation" of the Ames MGCM against recent data sets provided by the Mars Global Surveyor (MGS) spacecraft, currently in the mapping phase of its mission at Mars. Finally, an assessment of the simulated high-altitude wave activity during northern winter season has been conducted, and possible sources of the atmospheric variability have been identified.

a. Comparisons of Dynamical Cores: "B"- and "C"-Grids at L16

The radiative heating-cooling algorithms in the MGCM were extracted, and algorithms for simplified forcings in terms of spatially dependent thermal (Newtonian) relaxation rates and "radiative equilibrium" temperature fields for a specified season were inserted. In this approach, the prognostic equation for atmospheric temperature has the simple form $\partial T/\partial t \propto -\alpha_N(\varphi,\sigma)(T - \overline{T}_{eq}(\varphi,\sigma;L_s))$, where α_N is the relaxation rate; φ is latitude; and σ is the MGCM's vertical coordinate. The prescribed zonally symmetric radiative equilibrium thermal field as a function of latitude, height and season is independently determined using results from a 1-D radiative-convective model [cf. *Haberle et al.*, 1997a]. In addition, algorithms related to boundary-layer processes were extracted and a subroutine for a height dependent momentum dissipation (Rayleigh drag) was inserted. This required an additional term in the prognostic equations for horizontal momentum, namely $\partial v/\partial t \propto -\alpha_R(\varphi,\sigma)v$, where $v = (u,v)$ is the

horizontal wind vector, and α_R is the dissipation rate. In the dynamical-core simulations, the MGCM applied a "flat" lower boundary condition (i.e., no surface topography, thermal inertia and albedo). In addition, both models used the same vertical domain (L16) with a tropopause pressure $p_T = 1.0 \times 10^{-2}$ mbar (roughly 60 km), identical horizontal resolutions, $7.5°$ latitude $\times$ $9.0°$ longitude, the same horizontal "smoother" (an eigth-order Shapiro filter in longitude [*Shapiro*, 1970]), and nearly similar time differencing (a time step $\Delta t = 270$ s).

Several 50-day simulations have been performed for dust-free northern winter conditions using a moderate radiative-relaxation time constant (i.e., $L_s = 270°$, $\tau = 0$, $\tau_{radeq} = 2$ days). The prescribed radiative-equilibrium temperature field is identical to that presented in Figure 1a of *Haberle et al.* [1997a]. Shown in Figure 1 are time series of zonal (eastward) momentum taken in high northern latitudes and at upper levels of the model using either the old "B"-grid or new "C"-grid dynamical cores. It can be seen that on average, the "B"-grid is nearly twice as large and that instantaneous values can approach near-acoustic flow speeds, particularly at upper levels nearest the pole. The "C"-grid is genearlly less noisy.

Shown in Figures 2 and Figure 3 are latitude-pressure cross sections of the time and zonal average temperature and zonal wind from simulations using the "C"- and "B"-grid dynamical cores, respectively, as well as the unfiltered transient variability (indicated in color). The meridional cross sections indicate that most of the variability in the "C"-grid is concentrated in the middle and high latitudes of the northern hemisphere where a substantial meridional temperature gradient exists., In the presence of such strong temperature gradients and by thermal wind balance, a strong westerly jet develops in the extratropics which extend deep in the vertical (e.g., through 6–8 scale heights). The westerly jet core, $O(110$ m s$^{-1})$, is located just on the poleward side of the warm protrusion in midlatitudes. The latter results from compressional heating occurring within the descending branches of the Hadley circulation cells which emanates from low levels near the sub-solar point [*Zurek et al.*, 1992]. Comparisons of the same fields for the "B"-grid simulation (Figure 3) show a much "tighter" jet structure and "pockets" of high variability both in the winter baroclinic zone (where north-south thermal gradients are sharpest), as well as on the equatorward flank of the zonal jet. In the presence of very strong horizontal (zonal) shears, the latter region of variability may be associated with short-periods modes arising from symmetric instability. This characteristic is nearly absent in the "C"-grid simulation.

From these dynamical core simulations, we conclude that the "C"-grid is intrinsically smoother/less noisy than the "B"-grid and that patterns of the mean circulation, as well as its temporal variability, are for the most part rather similar.

b. Full-Up Mars GCM Comparisons: "B"- and "C"-Grids at L30

Using either the "C"- or "B"-grid dynamical core, the full-physics version of the Ames MGCM having 30 vertical levels (L30) has been applied in limited-season simulations (50-day integrations) centered around norther winter solstice and for weakly dusty conditions ($L_s = 270°$, $\tau = 0.3$). In these simulations, full surface variations are included (e.g., newly determined MGS/MOLA topography [*Smith et al.*, 1999] but with Mars Consortium thermal inertia and albedo). Aspects of the circulation's variability can be gathered from Figures 4 and Figure 5. Shown in each figure are the stationary temperature departure (i.e., the zonal RMS deviation from the time-mean temperature field, as determined by the last 30 days of the integration), and the transient temperature departure (i.e., the zonal RMS deviation from the instantaneous time departures that have been band-pass time filtered). The stationary circulation arises predominantly from fixed longitudinal variations in surface properties (e.g., topography and thermal contrasts), whereas the transient circulation (over the range of periods $O(2-10$ days), i.e., the synoptic-periods) is predominantly due to variability associated with transient baroclinic waves[*Barnes*, 1980; *Barnes et al.*, 1993].

Although slightly larger in midlatitudes, the stationary signal for these limited-season integrations (as measured by temperature perturbations) is generally similar for the "C"-grid (Figure 4a) compared to that seen in the "B"-grid (Figure 5a). This is broadly the same for the transient signal, however, the "C"-grid shows slightly weaker transient eddies (Figure 4b) compared to those simulated in the "B"-grid (Figure 5b). That the transient eddies are weaker in the "C"-grid simulation is most likely due to a slight weakening of the mean meridional baroclinicity (cf. Figure 2).

In addition, an annual simulation has been conducted using both the new "C"-grid and the old "B"-grid. Analyses for the southern winter solstice period for weakly dusty conditions ($L_s = 90°$, $\tau = 0.3$) are shown in Figures 6 and 7. The time and zonal average temperature and zonal wind fields from these simulations are remarkably similar, indicating peak westerly jets of $O(100 \text{ m s}^{-1})$ in the winter middle latitudes, and easterly jets of $O(-110 \text{ m s}^{-1})$ in the summer subtropics. Both simulations show a shallow westerly subtopical westerly jet in the summer hemisphere, as well as a weak high-latitude westerly jet. Furthermore, the strengths of the Hadley circulations are quite comparable as measured by the mean mass stream function with mass flux of $O(-25 \times 10^8 \text{ kg s}^{-1})$ (cf. Figures 6b and 7b).

Comparisons of eddy quantities show similarities as well for the "C"- and "B"-grid simulations, particularly stationary and transient variances of field variables (cf. Figures 6cd and 7cd). Again, the spatial patterns are quite identical although the transient temperature deviations are slightly weaker in the "C"-grid due most likely to a somewhat weaker baroclinicity in this simulation. Covariances of momentum and temperature (not shown) can indicate substantial differences in the magnitudes and spatial patterns, which may be due to the interpolation of the momentum onto a common reference grid (the "Π" points) used in the MGCM diagnostics routines. The exact differences need to be further assessed.

From these full-physics simulations with the MGCM, we conclude that the new "C"-grid produces rather similar climate statistics as produced by the old "B"-grid version of the model. This is encouraging in that the past modeling studies with the Ames MGCM have been performed using the "B"-grid [cf. *Pollack et al.* , 1990; *Haberle et al.* , 1993; *Barnes et al.* , 1993; *Murphy et al.*, 1995; *Hollingsworth et al.*, 1996; *Hollingsworth et al.*, 1997; *Joshi et al.*, 1997; *Haberle et al.* , 1999; etc], and as such, the conclusions from these investigations are most likely robust (i.e., discretization and other numerical artifacts are probably quite small). Thus, the utility of the "C"-grid version of the MGCM (e.g., a highly vectorized source code; far smoother prognostic meteorological fields; larger time stepping possible; varied horizontal/vertical resolution possible; capability of including N arbitrary passive tracers; horizontal grid rotations; etc) [*Suarez and Takacs*, 1995], can all be exploited in future-planned investigations related to Mars' climate, in particular, studies of the planet's water cycle and tracer/volatile transports.

c. Polar Vortex Dynamics: Heat Budgets and Angular Momentum Balances

We have also focused on key dynamical processes that determine the solstitial and equinoctial mean atmospheric thermal field on Mars, and by hydrostatic and geostrophic balances, the structure of its polar vortex. We have applied a high-top version of the MGCM (L30) in a series of mechanistic simulations for $L_s = 270°$ and $L_s = 30°$ where a variety of dust distributions are imposed, and components of the circulation are suppressed (e.g., the thermal tides, forced stationary planetary modes, etc). This approach is motivated by MGS/TES temperature retrievals [*Christensen et al.*, 1992; 1998] during Phase 1 and 2 aerobraking, and those obtained during the science phasing orbits (SPO). Analyses of the mean thermal structure and deduced (gradient-balanced) zonal-mean zonal wind fields have been conducted by *Conrath et al.* [1999]. In addition, a preliminary assessment of atmospheric wave phenomena (stationary and thermal tidal modes) for the pre-mapping phase has been conducted by *Banfield et al.* [1999]. Our mechanistic experiments with the MGCM arose particularly from TES observations

Exp. No.	Season (L_s)	τ_{max}	$\tau(\varphi)$	ν	Comments
99.01	270	0.3	no	0.03	benchmark
99.02	270	0.3	no	0.001	deep dust
99.03	270	0.3	no	0.01	moderately deep dust
99.04	270	0.3	$\cos\varphi$	0.03	no dust $\varphi \geq 65°N$
99.05	270	0.3	$\cos\varphi$	0.001	deep, none $\varphi \geq 65°N$
99.06	270	0.6	$\cos\varphi$	0.001	deep+, none $\varphi \geq 65°N$
99.07	270	0.6	no	0.001	deep+
99.08	270	0.6	$\cos\varphi$	0.001	nodiurnal cycle (but like 99.06)
99.14	270	0.6	$\cos\varphi$	0.001	nodiurnal cycle, flat topography

Table 1: Northern late autumn/early winter simulation cases with spatially-varying dust distributions.

during aerobraking Phase 1. A few additional experiments have been performed corresponding to the earliest stages of aerobraking Phase 2. The assumed dust initial conditions in these MGCM mechanistic experiments are listed in Table 1 and Table 2.

Results of the mean thermal structures and mean zonal winds for a selected set of the mechanistic experiments are shown in Figures 8 and 9. Comparisons of TES observations with the MGCM "benchmark" simulation (e.g., exp. no. 99.01) which assumed a shallower depth of the dust and a horizontally uniform distribution, indicated that the simulated subtropical atmosphere was $O(10–20\,K)$ too cold, and the extratropical warm "tongue" was completely missing. When the dust is assumed to vary in latitude (e.g., symmetric about the subsolar latitude but with dust absent in the polar night), and when it extends to higher altitude (e.g., exp. no. 99.06), the agreement with TES observations is much better. The resultant mean winds and temperatures in the simulations have been examined and the underlying thermodynamic balances have been diagnosed. Analyses of the wintertime experiments indicate that the net diabatic heating rate (solar and long wavelength) is balanced primarily by mean vertical advection (i.e., compressional heating in the winter extratropics), and that mean horizontal advection enhances the infrared cooling in the upper subtropics. An examination of heat (and momentum) flux convergences by eddies (e.g., short-period thermal tidal modes, synoptic-period transients, and quasi-stationary distur-

Exp. No.	Season (L_s)	τ_{max}	$\tau(\varphi)$	ν	Comments
99.09	30	0.2	no	0.01	moderately deep dust
99.10	30	0.2	$-0.4/\pi\varphi$	0.01	NH linear decrease with φ

Table 2: Northern early spring simulation cases with spatially-varying dust distributions.

bances) shows that there are significant cancellations between different circulation components which also act to balance the net diabatic heating. At this season, the eddy effects appear to produce a second-order "correction" to the heat balance set up by vertical (adiabatic) motions and diabatic heating. During spring, however (cf. Table 2), mean advections and eddy flux convergences are comparable, implying that all circulation components are active in the atmospheric heat balance.

In addition, consideration of the angular momentum budget in the mechanistic simulations shows that as the dust extends to higher altitude and has significant latitudinal variation, the overturning (i.e., Hadley) circulation becomes more angular momentum conserving, particularly below the 0.01 mbar level and in the wintertime sub- and extra-tropics. Taken together, in this way the MGCM can be used as an interpretive tool of the observations provided by MGS/TES, as well as those provided by MGS/RS.

d. High-Altitude Planetary Wave Propagation

The above mentioned mechanistic MGCM simulations have also been examined for high-altitude wave activity (e.g., traveling (transient) synoptic period modes, stationary modes and short-period thermal tidal modes). As shown in Figure 10, the stationary wave activity is found to maximize in the winter extratropics, particularly for the largest east-west (zonal) scales (e.g., $m = 1$ and $m = 2$). However, a rather surprising result came out of this suite of experiments having a deep and horizontally varying atmospheric dust loading (and thus an asymmetric diabatic heating field): significant stationary wave activity can also occur in the subtropics and summer hemisphere at high altitude. This wave activity occurs in a mean easterly zonal wind regime, and linear theory predicts that in fact, the shorter-scale planetary modes should be vertically and meridionally trapped (i.e., unable to obtain significant amplitude at high altitude) [*Andrews et al.*, 1987; *Hollingsworth and Barnes*, 1996]. This result appears to be robust in the high-top versions of the MGCM. It does not appear to be sensitive to the strength or domain depth of the Rayleigh friction ("sponge") layer assumed in the global climate model nor to the altitude of the model's top (assumed a rigid lid). These simulation results clearly indicate the importance of nonlinear interactions between the stationary components and other circulation (i.e., traveling and transient) components in the subtropics and at altitude. Stationary planetary wave calculations performed using a linear spherical primitive equations model show agreement in the winter hemisphere of vertical and meridional variations of wave amplitudes and phases compared to the fully nonlinear MGCM. The linear model differs in the summer hemisphere (where zonal-mean zonal winds are easterly), underscoring the importance of nonlinear effects in this hemisphere.

Preliminary analyses indicate the importance of the thermal tide in triggering the stationary wave activity in this region, via e.g., a modulation of a "localized" positive waveguide in the subtropics at certain longitudes at certain times of day that permits wave energy to "leak" from one hemisphere to the other. Shown in Figure 11 are stationary geopotential height amplitudes in the mechanistic experiment in which a diurnally-averaged solar heating is imposed (exp. no. 99.08). It can be seen that the stationary wave activity in the winter extratropics is rather similar; however, the summer subtropical activity is now absent (cf. Figure 10). A more quantitative assessment of the interhemispheric stationary wave transmission is indicated through analyses of the Eliassen-Palm flux and mean zonal wave driving (Figure 12). This diagnostic, under certain assumptions, can be shown to be indicative of the energy propagation (i.e., it is proportional to the group velocity of the disturbance). The top panel in Figure 12 (corresponding to exp. no. 99.06) shows tremendous stationary wave activity flux at high altitude from the summer subtropics toward the winter midlatitudes. The bottom panel (corresponding to exp. no. 99.08) shows very weak transmission in this same region. Other localized wave activity diagnostics, such as the Trenberth/Hoskins flux [*Trenberth*, 1986] that apply time filtering (e.g., high-pass and band-pass filtering to separate the short-period thermal tidal modes and synoptic-period transient disturbances) show similar results. Namely, the rectified effects from the short period modes produce a strong easterly torque on the mean westerly flow in the middle and high-latitude winter atmosphere.

3. PRESENTATIONS AND PUBLICATIONS

We list below titles of papers presented at national/international scientific conferences and of a manuscript submitted to the scientific literature during this JRI.

Hollingsworth, J.L.: "Studies of Mars' Atmosphere and Climate Using a Mars GCM: Support of the Mars Global Surveyor (MGS) Mission". Seminar presented at San Jose State University, Department of Meteorology, 6 November 1997.

Hollingsworth, J.L., R.M. Haberle, and J. Schaeffer: "Mars' Mean Atmospheric Thermal Structure: Preliminary Comparisons of MGS/TES Aerobraking Observations with a Mars GCM". Paper presented at a MGS Atmospheric Science Workshop, Jet Propulsion Laboratory, Pasadena, CA, 6 May 1998.

Hollingsworth, J.L.: "Mars GCM "B"- and "C"-Grid Comparisons". Presented at a UCLA ESM – NASA Ames MGCM Workshop, Department Atmospheric Sciences, UCLA, 2 November 1998.

Hollingsworth, J.L.: "Control Mechanisms and Seasonal Variations of Storm Tracks In Mars' Atmosphere". Presented at a UCLA ESM – NASA Ames MGCM Workshop, Department Atmospheric Sciences, UCLA, 2 November 1998.

Hollingsworth, J.L., R.M. Haberle, R.W. Zurek, and J. Schaeffer: "On Mars' Mean Atmospheric Thermal Structure: Sensitivity to Dust Loading, Net Diabatic Heating, and the Hadley Circulation" (*invited*). Paper presented at the XXIV EGS General Assembly, The Hague, The Netherlands, 19–23 April 1999.

Hollingsworth, J.L., R.M. Haberle, M.M. Joshi, J.R. Murphy, A.F.C. Bridger, and J. Schaeffer: "A Mars Climate Database: Results from the NASA Ames Mars Global Circulation Model". Paper presented at the XXIV EGS General Assembly, The Hague, The Netherlands, 19–23 April 1999.

Bridger, A.F.C., and J.L. Hollingsworth: "Stationary Large-Scale Wave Activity in Mars' Atmosphere". Paper presented at the XXIV EGS General Assembly, The Hague, The Netherlands, 19–23 April 1999.

Hollingsworth, J.L., R.M. Haberle, and J. Schaeffer: "Southern Hemisphere Storm Zones on Mars: Implications of MOLA Topography". Paper presented at the 5th International Conference on Mars, Caltech, Pasadena, CA, 19–23 July 1999.

Bridger, A.F.C., J.L. Hollingsworth, and R.M. Haberle: "Stationary Wave Activity Simulated by the NASA Ames MGCM Incorporating New MOLA Topography Data". Paper presented at the 5th International Conference on Mars, Caltech, Pasadena, CA, 19–23 July 1999.

Martin, T.Z., J.R. Murphy, and J.L. Hollingsworth: "Atmospheric Results from the MGS Horizon Science Experiment". Paper presented at the 5th International Conference on Mars, Caltech, Pasadena, CA, 19–23 July 1999.

Hollingsworth, J.L., P.B. James, and R.M. Haberle: "Modeling of Cyclo-, Fronto-genesis in the Mars Atmosphere". Paper presented at the XXXI Annual Meeting of the DPS, American Astronomical Society, Padova, Italy, 10–15 October 1999.

Bridger, A.F.C., and J.L. Hollingsworth: "High-Altitude Planetary Wave Propagation in Zonally Asymmetric Flows in Mars' Atmosphere". Paper presented at the XXXI Annual Meeting of the DPS, American Astronomical Society, Padova, Italy, 10–15 October 1999.

Joshi, M.M., J.L. Hollingsworth, R.M. Haberle, and A.F.C. Bridger, 2000: An interpretation of martian thermospheric waves based on analysis of a general circulation model. *Geophys. Res. Lett.*, **27**, 613–616.

and the following manuscripts are planned for 2000:

Hollingsworth, J.L., R.M. Haberle, R.W. Zurek, and J. Schaeffer: "On Mars' Mean Atmospheric Thermal Structure: Sensitivity to Dust Loading, Net Diabatic Heating, and the Hadley Circulation". To be submitted to *Icarus.*

Hollingsworth, J.L., and D.P. Hinson: "Forced Rossby Wavetrains During Late Northern Spring on Mars". To be submitted to *J. Geophys. Res.*

REFERENCES

Andrews, D. G., J. R. Holton, and C. B. Leovy, 1987: *Middle Atmosphere Dynamics*, Academic Press, 489 pp.

Arakawa, A., and V.R. Lamb, 1977: Computational design of the basic dynamical processes of the UCLA general circulation model. In *Methods in Computation Physics: General Circulation Models of the Atmosphere*, **17**, B. Adler, J. Chang, S. Fernbach, and M. Rotenberg, Eds., Academic Press, 173–265.

Banfield, D.B. J. Conrath, J.C. Pearl, M.D. Smith, P. Christensen, 2000: Thermal tides and stationary waves on Mars as revealed by MGS TES. Submitted to *J. Geophys. Res.'*

Barnes, J.R., 1980: Time spectral analysis of midlatitude disturbances in the Martian atmosphere. *J. Atmos. Sci.,* **37,** 2002–2015.

Barnes, J.R., J.B. Pollack, R.M. Haberle, R.W. Zurek, C.B. Leovy, H. Lee, and J. Schaeffer, 1993: Mars atmospheric dynamics as simulated by the NASA-Ames general circulation model II. Transient baroclinic eddies. *J. Geophys. Res.,* **98,** 3125–3148.

Christensen, P. R., D. L. Anderson, S. C. Chase, R. N. Clark, H. H. Kieffer, M. C. Malin, J. C. Pearl, J. Carpenter, N. Bandiera, F. G. Brown, and S. Silverman, 1992: Thermal emission spectrometer experiment: Mars Observer mission. *J. Geophys. Res.,* **97,** 7719–7734.

Christensen, P. R., D. L. Anderson, S. C. Chase, R. T. Clancy, R. N. Clark, B. J. Conrath, H. H. Kieffer, R. O. Kuzmin, M. C. Malin, J. C. Pearl, T. L. Roush, M. D. Smith, 1998: Results from the Mars Global Surveyor thermal emission spectrometer. *Science,* **279,** 1692–1698.

Conrath, B.J., J.C. Pearl, M.D. Smith, W.C. Maguire, P.R. Chirstensen, S. Dason, and M.S. Kaelberer, 2000: Mars Global Surveyor thermal emission spectrometer (TES) observations: Atmospheric temperatures during aerobraking and science phasing. Submitted to *J. Geophys. Res.*

Farmer, C.B., D.W. Davies, A.L. Holland, D.D. LaPorte, and P.E. Doms, 1977: Mars: Water vapor observations from the Viking orbiters. *J. Geophys. Res.,* **82,** 4225–4248.

Haberle, R.M., J.B. Pollack, J.R. Barnes, R.W. Zurek, C.B. Leovy, J.R. Murphy, H. Lee, and J. Schaeffer, 1993: Mars atmospheric dynamics as simulated by the NASA-Ames general circulation model I. The zonal-mean circulation. *J. Geophys. Res.,* **98,** 3093–3124.

Haberle, R.M., H. Houben, J.R. Barnes, and R.E. Young, 1997a: A simplified three-dimensional model for Martian climate studies. *J. Geophys. Res.,* **102,** 9051–9067.

Haberle, R.M., J.R. Barnes, J.R. Murphy, M.M. Joshi, and J. Schaeffer, 1997b: Meteorological predictions for the Mars Pathfinder lander. *J. Geophys. Res.*, **102**, 13301–13311.

Haberle, R.M., M.M. Joshi, J.R. Murphy, J.R. Barnes, J.T. Schofield, G. Wilson, M. Lopez-Valverde, J.L. Hollingsworth, A.F.C. Bridger, and J. Schaeffer, 1999: GCM simulations of the Mars Pathfinder ASI/MET data. *J. Geophys. Res.*, **104**, 8957–8974.

Hollingsworth, J.L., and J.R. Barnes, 1996: Forced stationary planetary waves in Mars' winter atmosphere. *J. Atmos. Sci.*, **53**, 428–448.

Hollingsworth, J.L., R.M. Haberle, J.R. Barnes, A.F.C. Bridger, J.B. Pollack, H. Lee, and J. Schaeffer, 1996: Orographic control of storm zones on Mars. *Nature*, **380**, 413–416.

Hollingsworth, J.L., R.M. Haberle, and J. Schaeffer, 1997a: Seasonal variations of storm zones on Mars. *Adv. Space Res.*, **19**, 1237–1240.

Hollingsworth, J.L., R.M. Haberle, and J. Schaeffer, 1997b: Control mechanisms and seasonal variations of storm tracks in Mars' atmosphere. *Annales Geophysicae*, **100**, C464.

Holton, J.R. 1992: *An Introduction to Dynamic Meteorology*, Academic Press, 511 pp.

Houben, H.C., R.M. Haberle, R.E. Young, and A.P. Zent, 1997: Modeling the Martian seasonal water cycle. *J. Geophys. Res.*, **102**, 9069–9083.

James, P.B., J.F. Bell, R.T. Clancy, S.W. Lee, L.J. Martin, and M.J. Wolff, 1996: Global imaging of Mars by Hubble Space Telescope during the 1995 opposition. *J. Geophys. Res.*, **101**, 18883–18890.

Jakosky, B.M., 1985: The seasonal cycle of water on Mars. *Space Sci. Rev.*, **41**, 131–200.

Jakosky, B.M., and C.B. Farmer, 1982: The seasonal and global behavior of water vapor in the Mars atmosphere: Complete global results of the Viking atmospheric water detector experiment. *J. Geophys. Res.*, **87**, 2999–3019.

Jakosky, B.M., and R.M. Haberle, 1992: The seasonal behavior of water on Mars. *Mars*, H.H. Kieffer, B.M. Jakosky, C.W. Snyder, and M.S. Matthews, Eds., University of Arizona Press, 969–1016.

Joshi, M.M., S.R. Lewis, P.L. Read, and D.C. Catling, 1995: Western boundary currents in the Martian atmosphere: Numerical simulations and observational evidence. *J. Geophys. Res.*, **100**, 5485–5500.

Joshi, M.M., R.M. Haberle, J.R. Barnes, J.R. Murphy, and J. Schaeffer, 1997: Low-level jets in the NASA Ames Mars general circulation model. *J. Geophys. Res.*, **102**, 6511–6524.

Kieffer, H.H., 1979: Mars south polar spring and summer temperatures: A residual CO_2 frost. *J. Geophys. Res.*, **84**, 8263–8288.

Mellor, G.L., and T. Yamada, 1982: Development of a turbulence closure model for geophysical fluid problems. *Rev. Geophys. Space Phys.*, **20**, 851–875.

Murphy, J.R., J.B. Pollack, R.M. Haberle, C.B. Leovy, O. B. Toon, and J. Schaeffer, 1995: Three-dimensional numerical simulation of Martian global dust storms. *J. Geophys. Res.*, **100**, 26357–26376.

Pollack, J.B., R.M. Haberle, J. Schaeffer, and H. Lee, 1990: Simulations of the general circulation of the Martian atmosphere I: Polar processes. *J. Geophys. Res.*, **95**, 1447–1473.

Rind, D., R. Suozzo, N.K. Balachandran, A. Lacis, and G. Russell, 1988: The GISS global climate-middle atmosphere model. Part 1: Model structure and climatology. *J. Atmos. Sci.*, **45**, 329–370.

Rind, D., R. Suozzo, and N.K. Balachandran, 1988: The GISS global climate-middle atmosphere model. Part 2: Model variability due to interactions between planetary waves, the mean circulation and gravity wave drag. *J. Atmos. Sci.*, **45**, 371–386.

Shapiro, R., 1970: Smoothing, filtering and boundary effects. *Rev. Geophys. Space Phys.*, **8**, 359–387.

Smith, D.E., and co-authors, 1999: The global topography of Mars and implications for surface evolution. *Science,* **284**, 1495–1503.

Suarez, M.J., and, L.L. Takacs, 1995: "Documentation of the ARIES/GEOS Dynamical Core: Version 2", In *Technical Report Series on Global Modeling and Data Assimilation,* **5**, NASA Technical Memorandum 104606, 45 pp.

Trenberth, K. E., 1986: An assessment of the impact of transient eddies on the zonal flow during a blocking episode using localized Eliassen-Palm flux diagnostics. *J. Atmbs. Sci.*, **43**, 2070–2087.

Zurek, R.W., J.R. Barnes, R.M. Haberle, J.B. Pollack, J.E. Tillman, and C.B. Leovy, 1992: Dynamics of the atmosphere of Mars. *Mars*, H.H. Kieffer, B.M. Jakosky, C.W. Snyder, and M.S. Matthews, Eds., University of Arizona Press, 835–933.

G20L16 Dynamical Core Tests

AMES/MGCM vs GSFC/ARIES: U(I=28,J=22,L), Ls = 270, radeqtc = 2 day

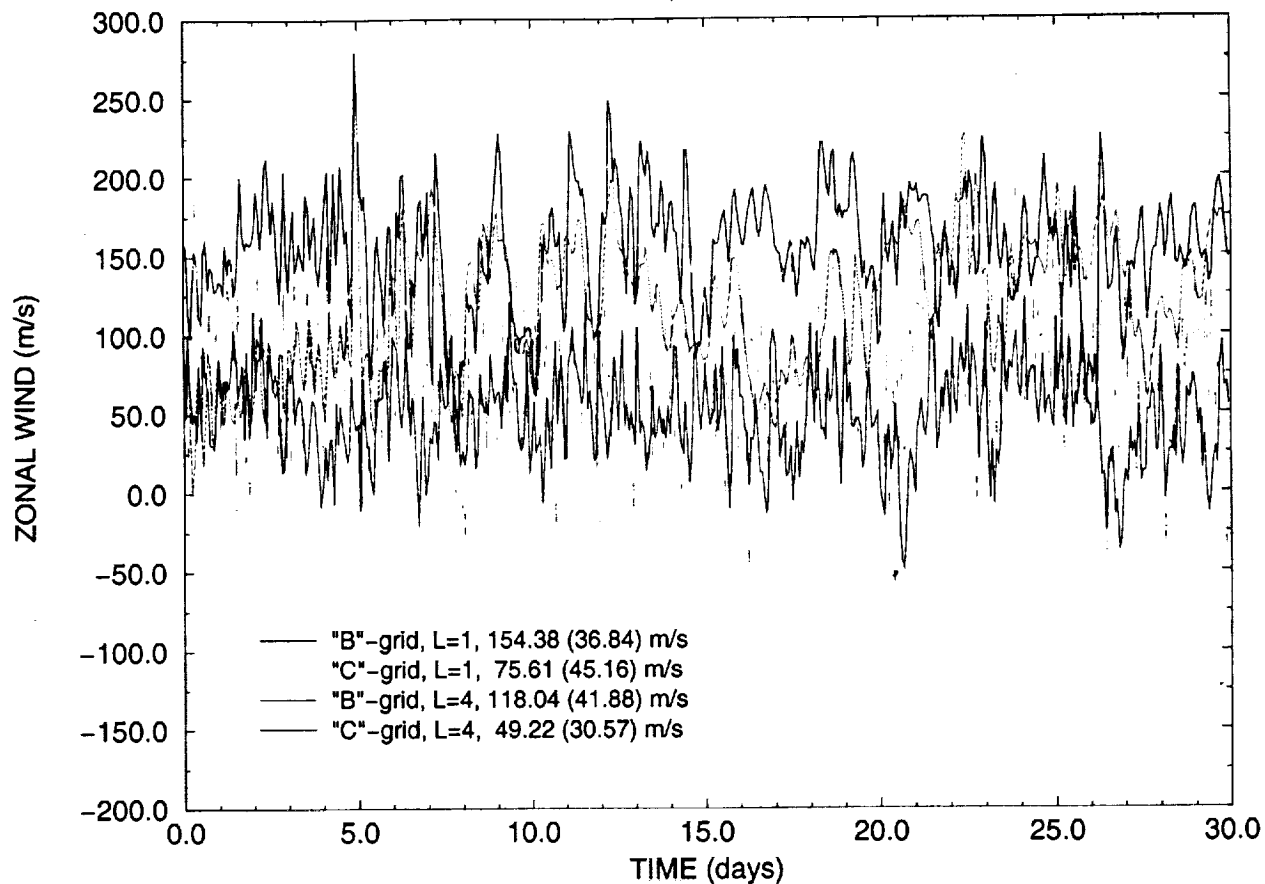Figure 1: Time series of zonal wind at a test grid point (67.5°E, 71.3°N) at layer 1 and layer 4 for the "B"-grid and "C"-grid dynamical cores for a simulation using a northern winter solstice no-dust radiative-equilibrium field (i.e., $L_s = 270°$, $\tau = 0$, $\tau_{radeq} = 2$ days).
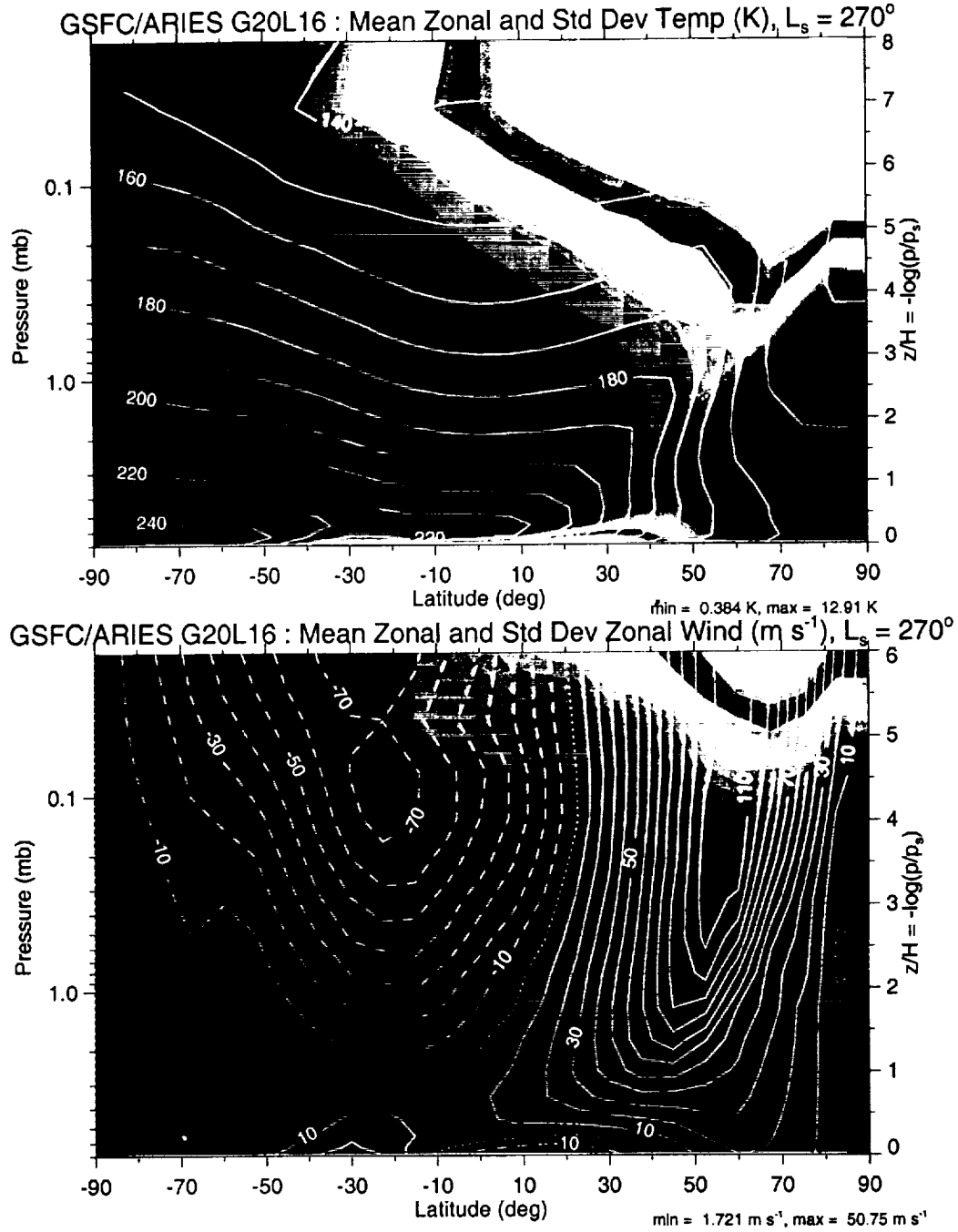
Figure 2: A Mars climate simulation using the GSFC/ARIES "C"-grid dynamical core at 7.5 × 9.0° horizontal resolution and 16 vertical (σ) layers (without surface topography) using the $L_s = 270°$, $\tau = 0$ radiative-equilibrium relaxation field with a relaxation time constant $\tau_{radeq} = 2$ days: time and zonally averaged (a) temperature (K) and (b) zonal wind (m s^{-1}). The contour interval in (a) is 10 K. Solid (dashed) contours in (b) correspond to eastward (westward) wind and the dotted contour is the zero isopleth. The contour interval is 10 m s^{-1}. In panels (a) and (b), the color background fields correspond to the transient RMS temperature and zonal wind departures, respectively.
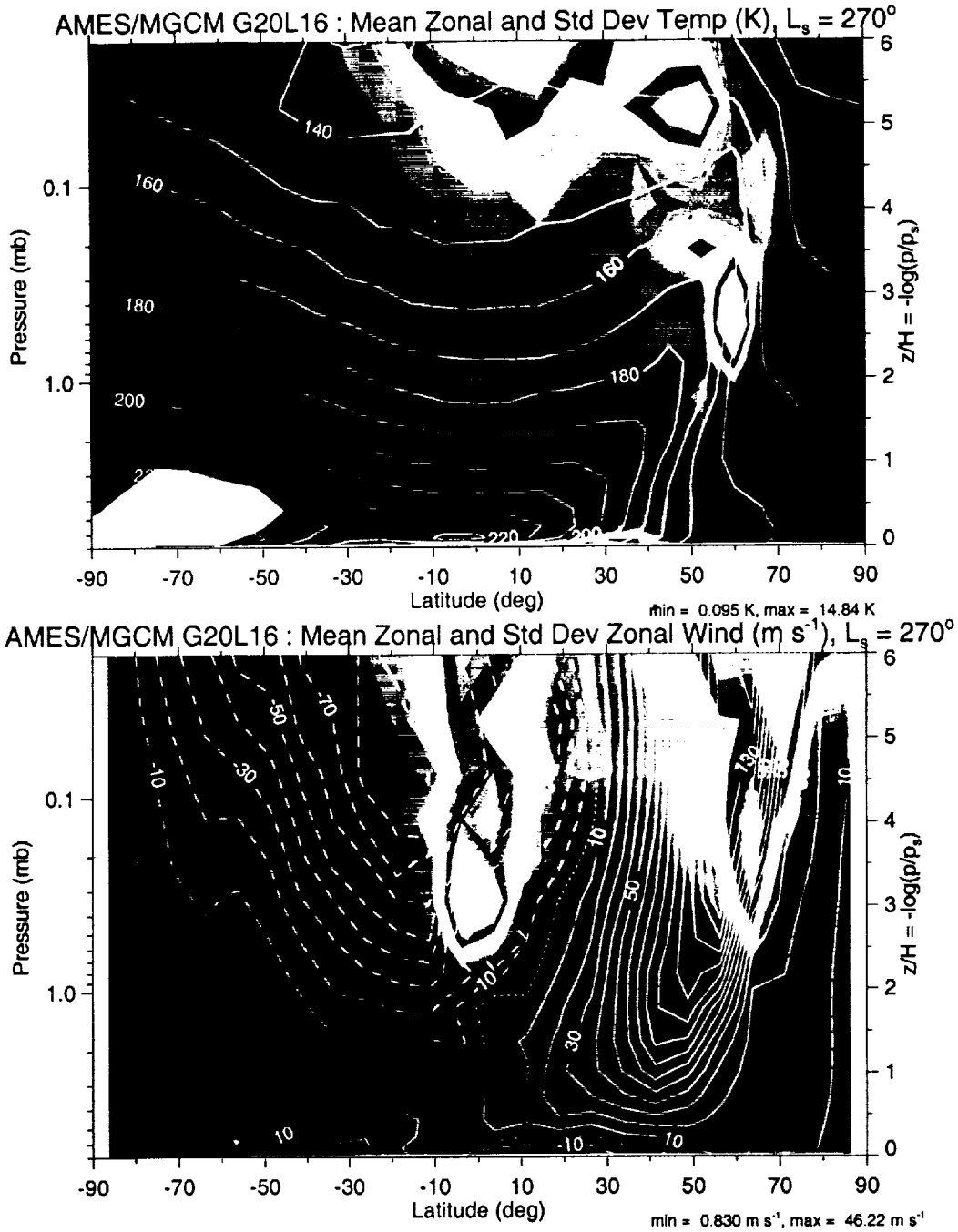
AMES/MGCM G20L16 : Mean Zonal and Std Dev Temp (K), L$_s$ = 270°

min = 0.095 K, max = 14.84 K

AMES/MGCM G20L16 : Mean Zonal and Std Dev Zonal Wind (m s^{-1}), L$_s$ = 270°

min = 0.830 m s^{-1}, max = 46.22 m s^{-1}

Figure 3: A Mars climate simulation using the NASA/Ames "B"-grid dynamical core at 7.5 × 9.0° horizontal resolution and 16 vertical (σ) layers (without surface topography) using the L_s = 270°, $\tau = 0$ radiative-equilibrium relaxation field with a relaxation time constant τ_{radeq} = 2 days: time and zonally averaged (a) temperature (K) and (b) zonal wind (m s^{-1}). The contour interval in (a) is 10 K. Solid (dashed) contours in (b) correspond to eastward (westward) wind and the dotted contour is the zero isopleth. The contour interval is 10 m s^{-1}. In panels (a) and (b), the color background fields correspond to the transient RMS temperature and zonal wind departures, respectively.
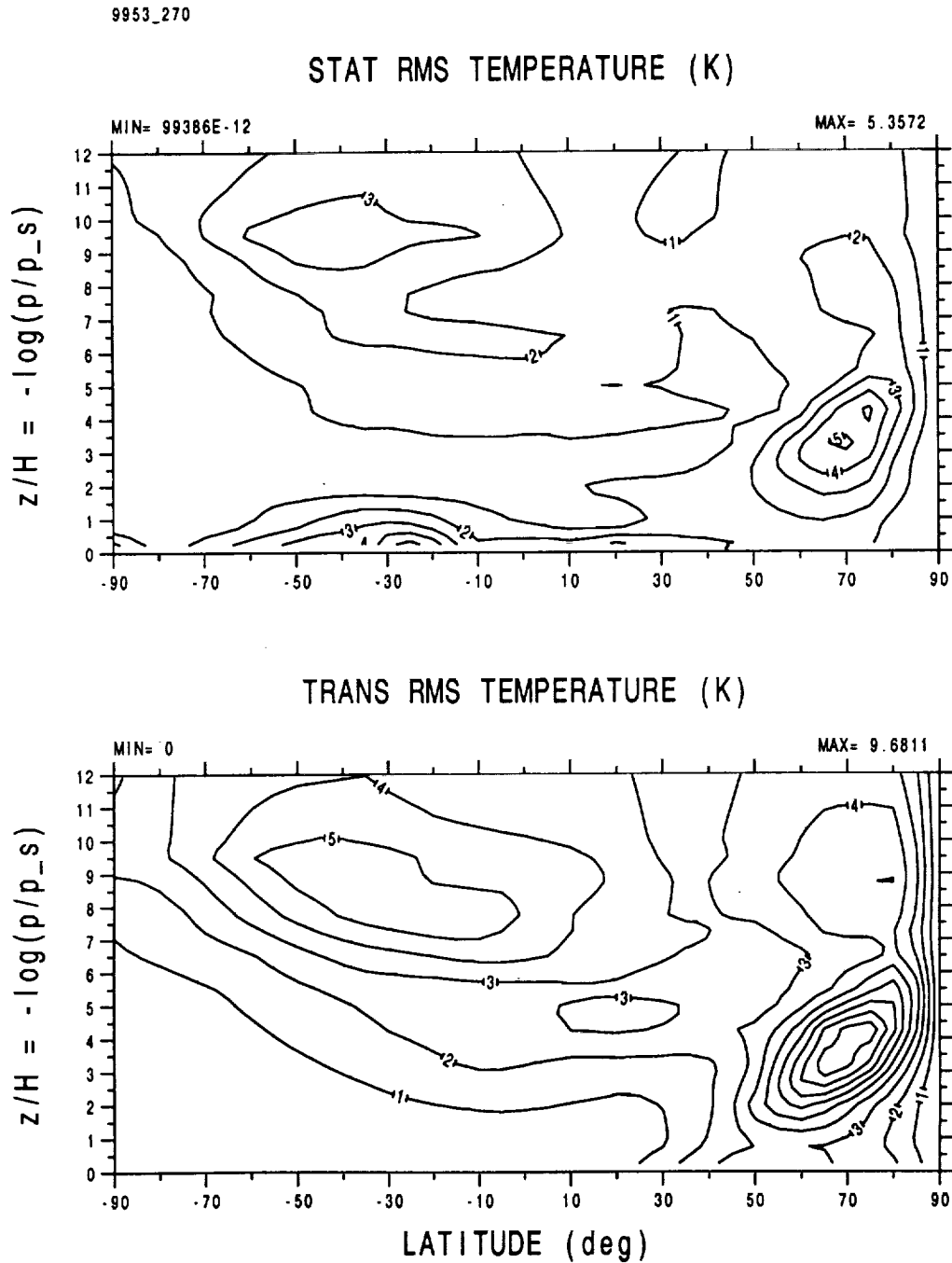
9953_270

STAT RMS TEMPERATURE (K)

MIN= 99386E-12

MAX= 5.3572

TRANS RMS TEMPERATURE (K)

MIN= 0

MAX= 9.6811

LATITUDE (deg)

Figure 4: Circulation statistics from a 50-day simulation for northern winter solstice ($L_s = 270°$, $\tau = 0.3$) using the Mars GCM with the "C"-grid (zonal RMS quantities): (a) stationary temperature (K) and (b) band-pass filtered transient temperature (K). The contour interval is 1 K in panels (a) and (b).
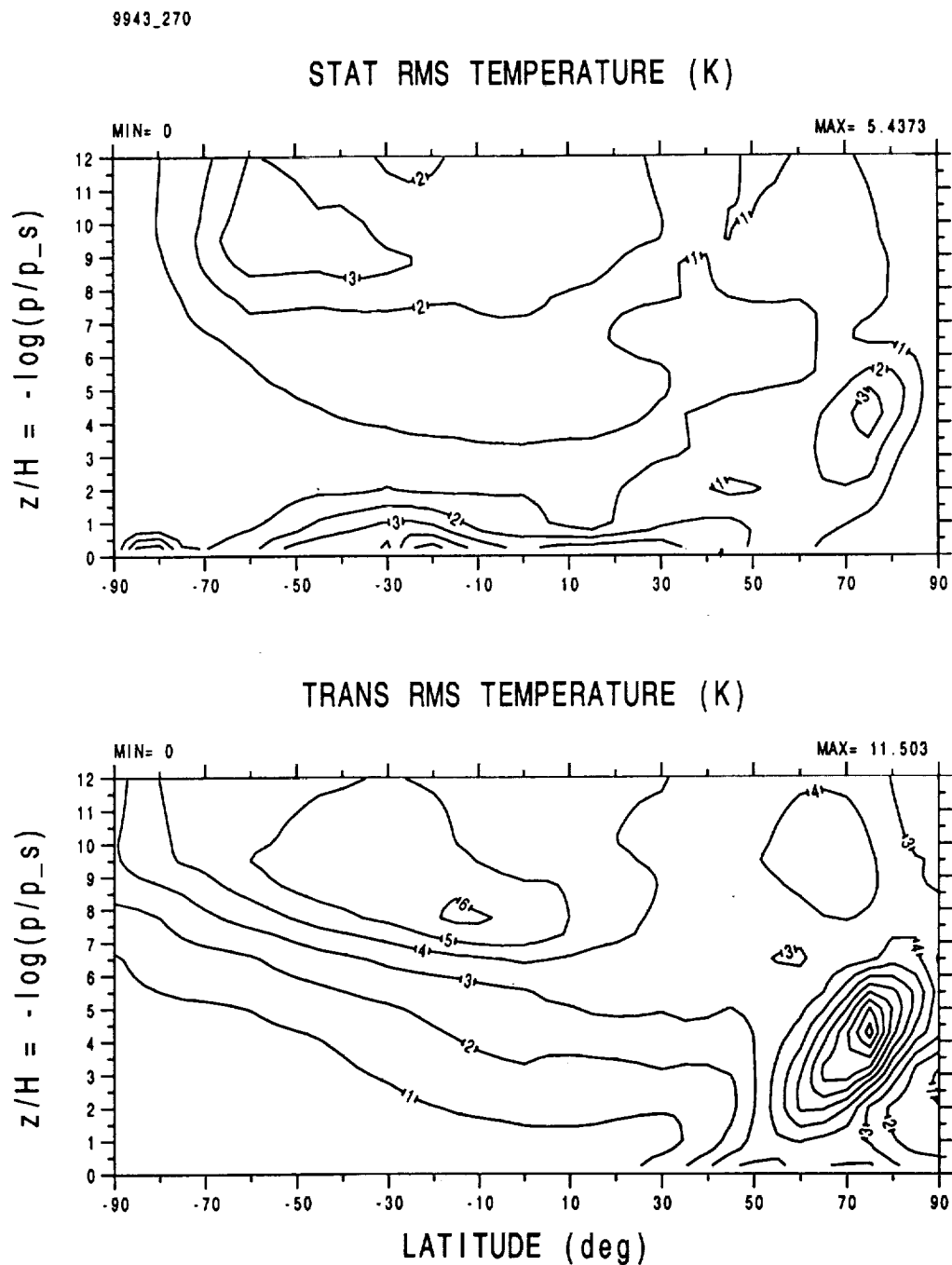
9943_270

STAT RMS TEMPERATURE (K)

MIN= 0   MAX= 5.4373

TRANS RMS TEMPERATURE (K)

MIN= 0   MAX= 11.503

LATITUDE (deg)

Figure 5: As in Figure 4 but using the Mars GCM with the "B"-grid (zonal RMS quantities): (a) stationary temperature (K) and (b) band-pass filtered transient temperature (K). The contour interval is 1 K in panels (a) and (b).

9976_090

ZONAL-MEAN ZONAL WIND (ms⁻¹) AND TEMP (K)

ZONAL-MEAN MASS STRM FUNC (10⁸ kgs⁻¹)
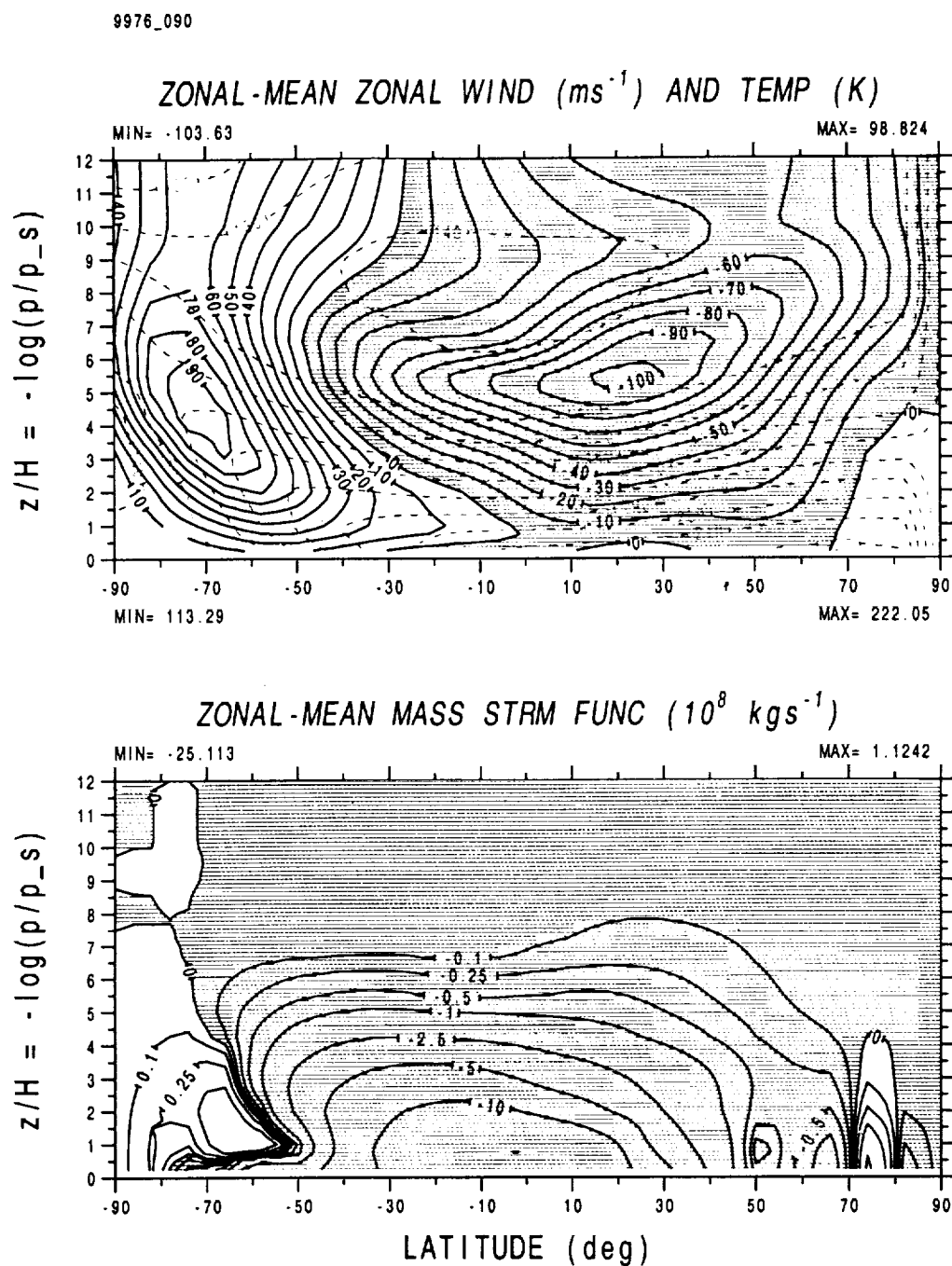
Figure 6: Circulation statistics from an annual simulation for southern winter solstice ($L_s = 90°, \tau = 0.3$) using the Mars GCM with the "C"-grid: (a) time and zonal average zonal wind (m s⁻¹) and temperature (K) (red dashed contours); (b) time and zonal average mass stream function ($\times 10^8$ kg s⁻¹). In panel (a), the zonal wind contour interval is 10 m s⁻¹ with negative (westward) values shaded green, and the temperature contour interval is 10 K; in panel (b) the stream function contour interval is nonuniform.

9976_090

STAT RMS TEMPERATURE (K)

MIN= 0   MAX= 11.602

TRANS RMS TEMPERATURE (K)

MIN= 0   MAX= 2.8773
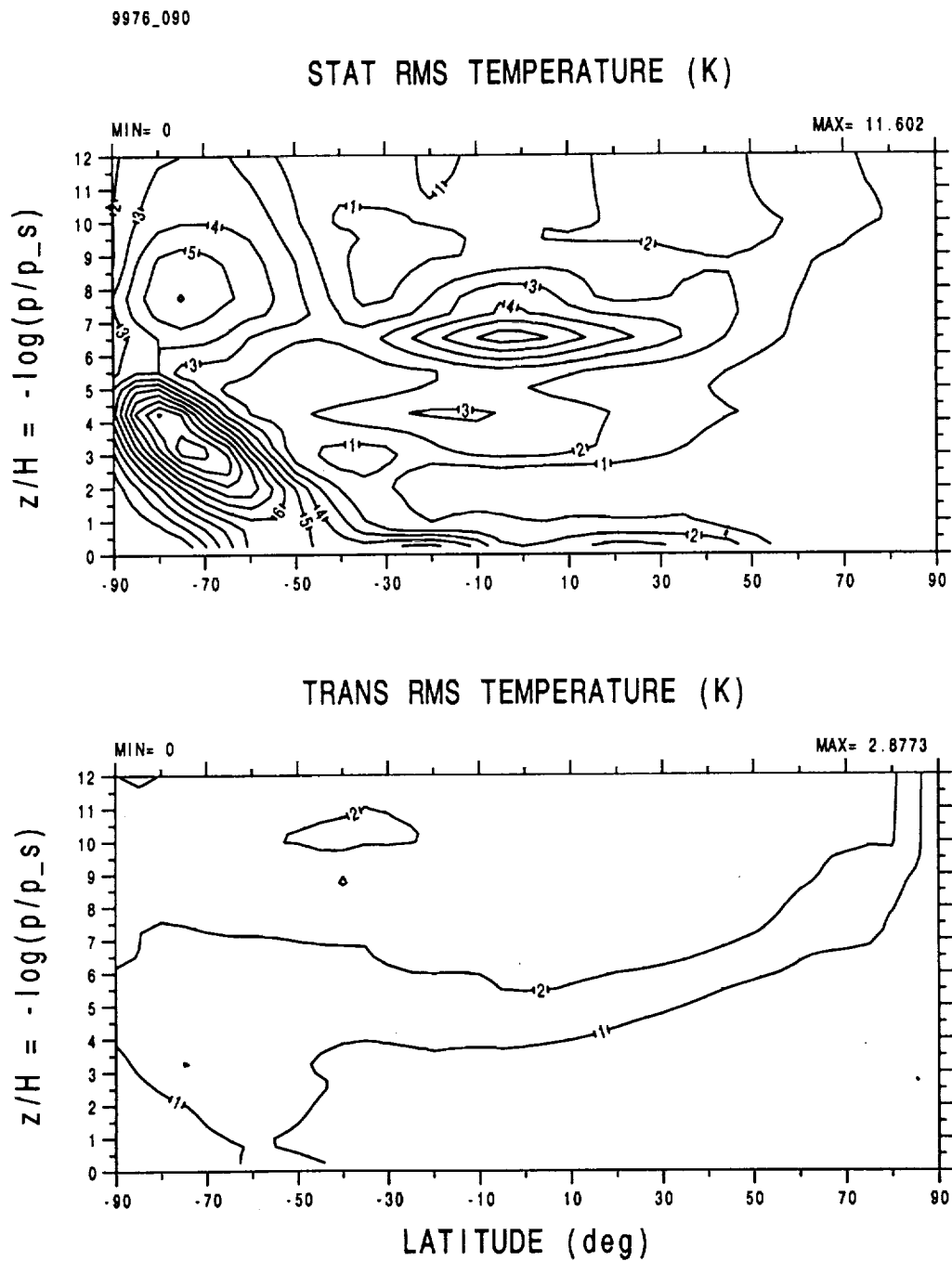

LATITUDE (deg)

Figure 6: (continued) The zonal RMS (c) stationary and (d) band-pass filtered transient temperature (K). The contour interval is 1 K in panels (c) and (d).
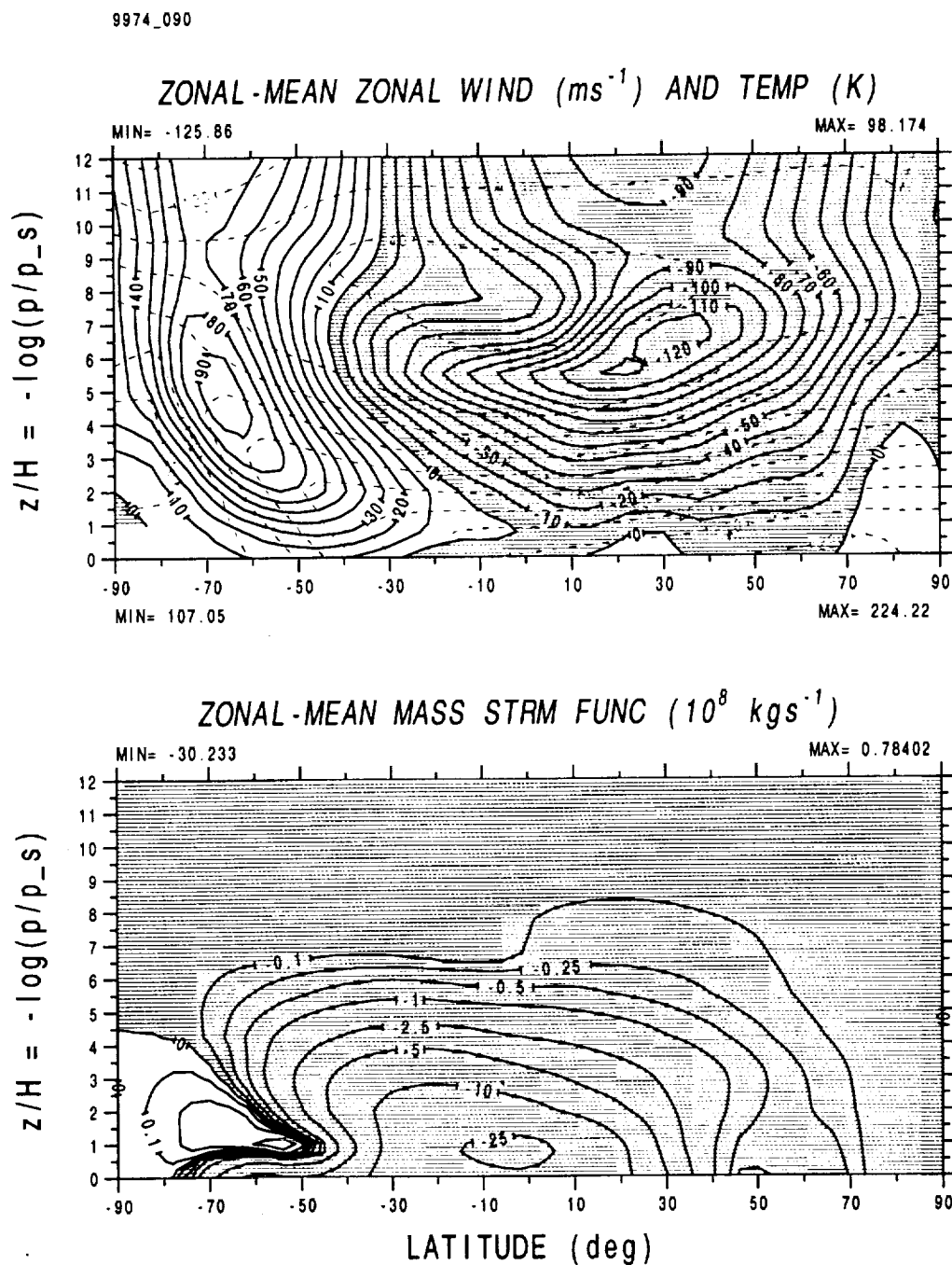
9974_090

ZONAL-MEAN ZONAL WIND (ms^{-1}) AND TEMP (K)

MIN= -125.86   MAX= 98.174

MIN= 107.05   MAX= 224.22

ZONAL-MEAN MASS STRM FUNC $(10^8 \ kgs^{-1})$

MIN= -30.233   MAX= 0.78402

LATITUDE (deg)

Figure 7: As in Figure 6 but from an annual simulation for southern winter solstice ($L_s = 90°$, $\tau = 0.3$) using the Mars GCM with the "B"-grid
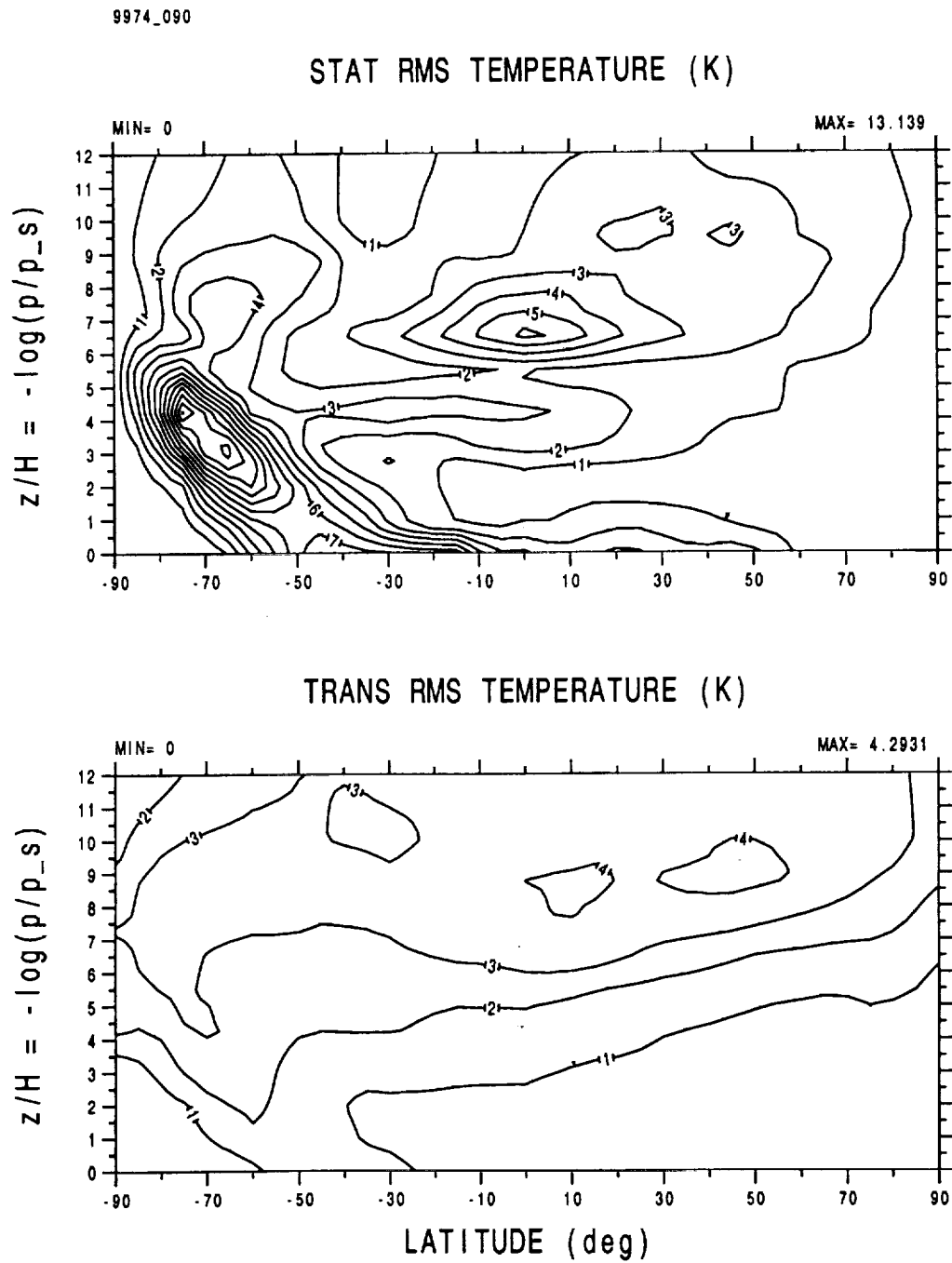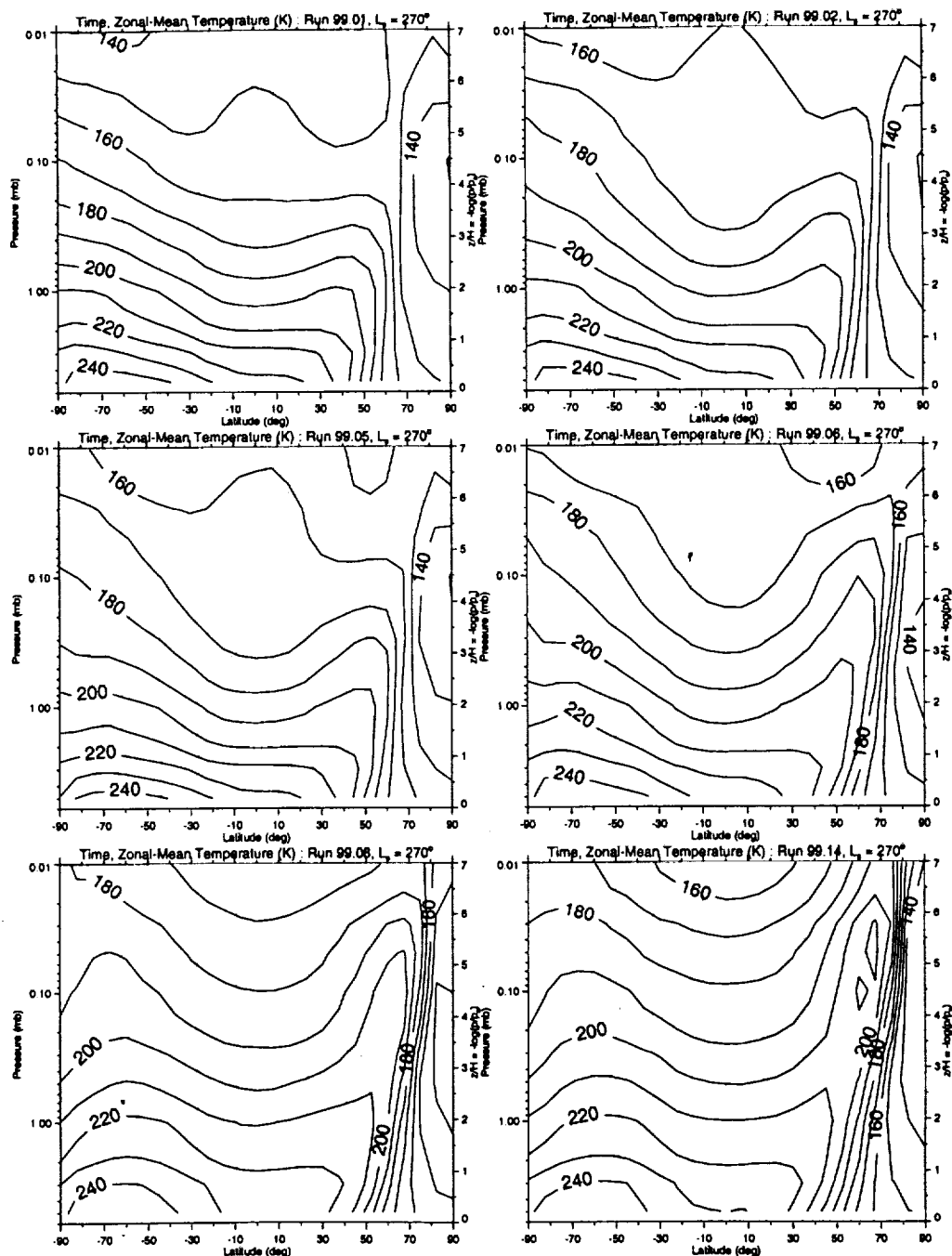
9974_090

STAT RMS TEMPERATURE (K)

MIN= 0

MAX= 13.139

TRANS RMS TEMPERATURE (K)

MIN= 0

MAX= 4.2931

LATITUDE (deg)

Figure 7: (continued)

Figure 8: The time and zonally averaged temperature (K) for late northern autumn, early winter ($L_s = 260$–$280°$) Mars GCM simulations having various assumed spatial distributions of atmospheric dust (cf. Table 1). The contour interval is 10 K in all panels.
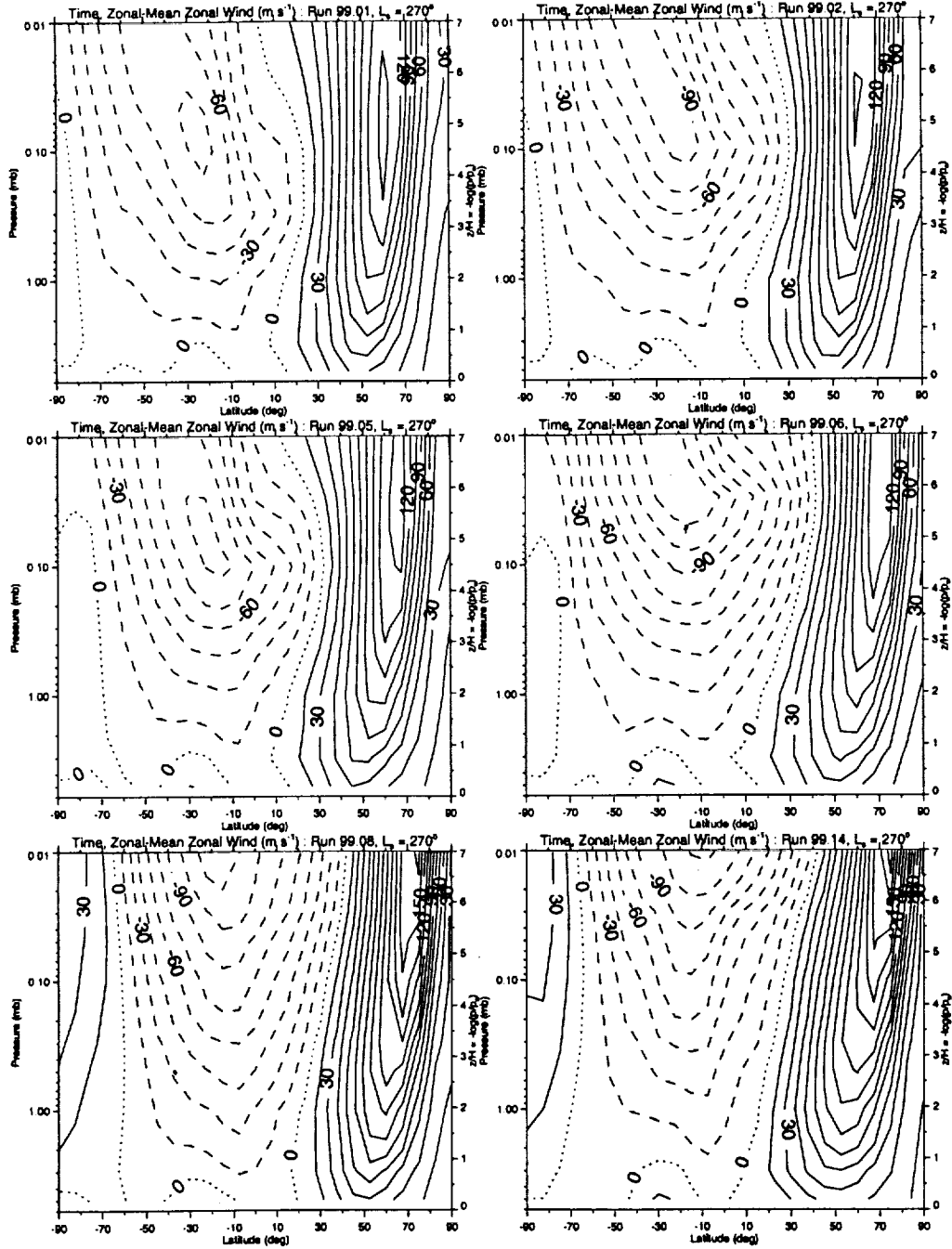
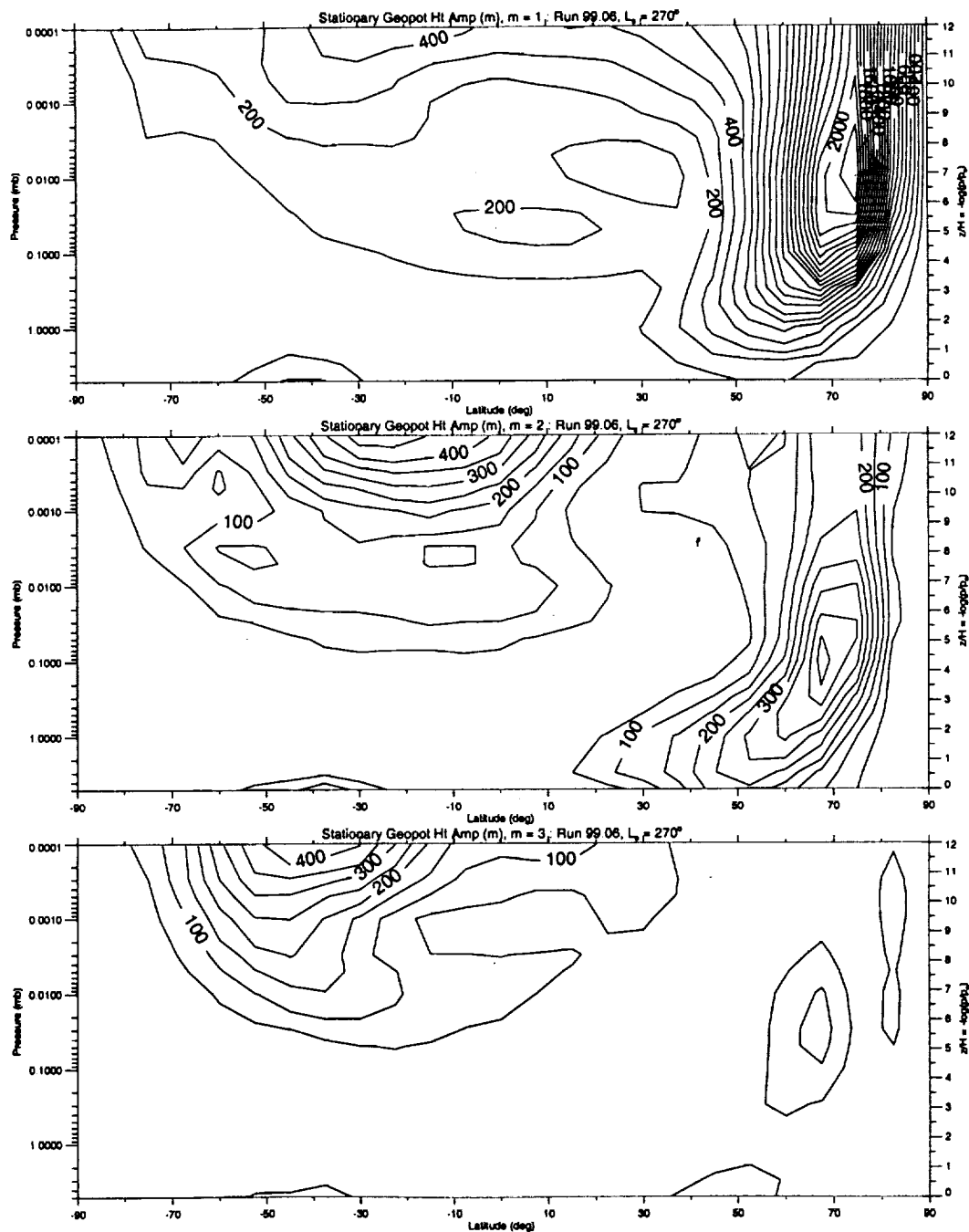Figure 9: As in Figure 8 but for the time and zonally averaged zonal wind (m s^{-1}). The contour interval is 15 m s^{-1} in all panels.

Figure 10: Stationary geopotential height (m) for a late northern autumn, early winter ($L_s = 260–280°$) Mars GCM simulation (exp. no. 99.06) that has spatially varying dust, full surface variations and a full diurnal cycle. The contour interval is 100 m in (a), and 50 m in (b) and (c).
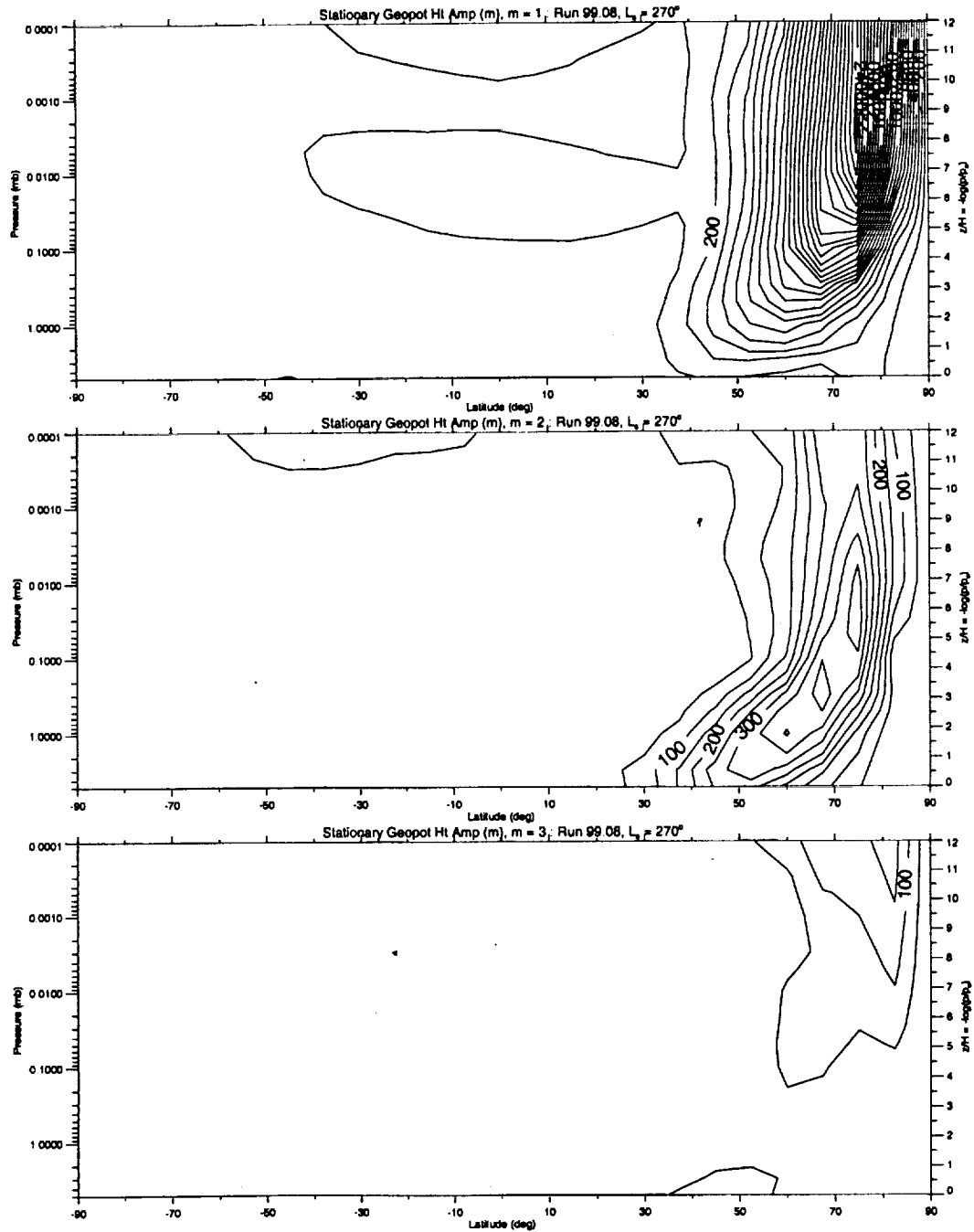
Figure 11: As in Figure 10 but for the experiment with a diurnally-averaged solar heating (exp. no. 99.08). The contour interval is 100 m in (a), and 50 m in (b) and (c).
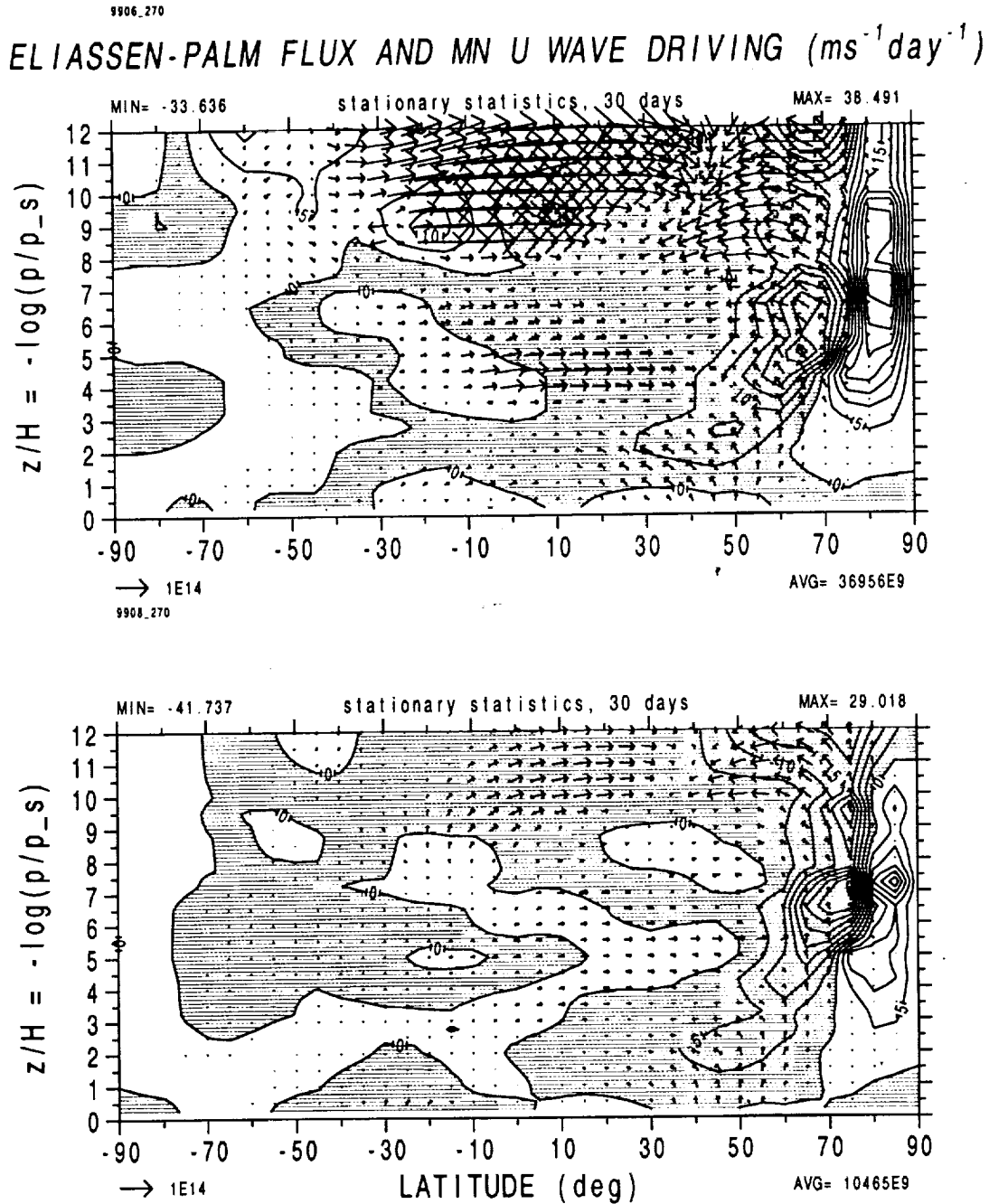
9906_270

ELIASSEN-PALM FLUX AND MN U WAVE DRIVING $(ms^{-1}day^{-1})$

9908_270

Figure 12: Eliassen-Palm (EP) flux, $\mathbf{F} = (0, F^{(\varphi)}, F^{(z)})$, and the mean zonal wave driving, $D_F = (\rho_0 a \cos\varphi)^{-1}(\nabla \cdot \mathbf{F})$ (m s^{-1} day^{-1}) for the experiments shown in Figures 3 and 4. (a) spatially varying dust, full surface variations and a full diurnal cycle (exp. no. 99.06) and (b) spatially varying dust, full surface variations and a diurnally-averaged solar heating (exp. no. 99.08). The green shading corresponds to negative wave driving (i.e., a deceleration of the mean zonal flow) and the contour interval is 5 m s^{-1} day^{-1}.